Available online at www.sciencedirect.com
SCIENCE DIRECT®
Pergamon
Acta Materialia XX (2003) XXX–XXX
Acta MATERIALIA
www.actamat-journals.com

Diffusionally accommodated interfacial sliding in metal-silicon systems

K.A. Peterson [a], I. Dutta [a,*], M.W. Chen [b]

[a] *Center for Materials Science and Engineering, Department of Mechanical Engineering, Naval Postgraduate School, Monterey, CA 93943, USA*
[b] *Department of Mechanical Engineering, Johns Hopkins University, Baltimore, MD 21218, USA*

Received 8 January 2002; received in revised form 6 February 2003; accepted 7 February 2003

Abstract

The kinetics and mechanism of diffusionally accommodated interfacial sliding (interfacial creep) under far-field shear and normal stresses was studied, based on diffusion-bonded Al-Si-Al sandwich specimens. A previously developed interfacial creep law [Funn and Dutta, Acta Mater 1999; 47: 149], which proposed that interfaces may slide via interface-diffusion controlled diffusional creep, was experimentally validated by carrying out a systematic parametric study. In agreement with the model, the Si-Al interfaces slid via diffusional creep ($n = 1$) under the influence of an effective shear stress, which depends on the far-field shear and normal stresses, as well as the interfacial topography. Compressive stresses acting normal to the interface lowered the effective shear stress, resulting in a threshold effect, thus reducing the sliding rate. The rate of sliding was controlled by diffusional mass transport through a thin amorphous, O-rich interfacial layer, under the influence of local interfacial stress gradients, which arose due to the topological features of the interface. Instances of interfacial sliding in the absence of interfacial de-cohesion, which have been noted in composites, thin-film systems, etc., may be explained by the present mechanism, which also offers an alternative rationalization of threshold behavior during diffusional flow (besides interface-reaction control).

Keywords: Interfacial sliding; Diffusional creep; Threshold stress; Interfacial topography

1. Introduction

The mechanical properties of interfaces between dissimilar materials at elevated temperature are critical to the performance of a wide range of engineering systems. Interfaces of interest include those in composites, multi-layers, thin-film/substrate systems, and microelectronic devices and packages. In many such applications, large shear stresses may develop at interfaces during thermo-mechanical excursions when the difference in coefficient of thermal expansions (CTE) between the materials is large, and at least one of the materials adjoining the interface is subjected to a high homologous temperature (T/T_m). This enables *diffusionally accommodated sliding* processes (interfacial creep) to occur at the interface

* Corresponding author. Tel.: +1 831-656-2851; fax: +1-831-656-2238.
E-mail address: idutta@nps.navy.mil (I. Dutta).

1359-6454/03/$30.00 © 2003 Published by Elsevier Science Ltd on behalf of Acta Materialia Inc.
doi:10.1016/S1359-6454(03)00088-0

[e.g., 1–7]. Most typically, interfacial shear stresses are confined to the extremities of one of the components, such as fiber-ends in a composite, or the edges of a thin film on a substrate [e.g., 2,8], limiting the impact of interfacial creep. However, when one of the phases is dimensionally small (e.g., narrow metallic thin film lines on a substrate) shear stresses may prevail over a large area fraction of the total interface, and interfacial creep may severely impact the dimensional stability or reliability of the component of interest. With the continuing trend towards miniaturization of components with numerous multi-material interfaces in microelectronics, micro-electromechanical systems (MEMS), etc., interfacial sliding is likely to play an increasingly important role, making it imperative to develop a mechanistic understanding of this phenomenon.

Direct evidence of interfacial creep has been observed in continuous fiber composites [1–3], thin film/substrate systems [5–7], and back-end structures in microelectronic devices [4,9]. In composites, interfacial creep manifests itself as strain incompatibilities between matrix and fiber following thermal cycling [1,3]. In film-substrate systems, it causes alteration of the film footprint on the substrate [6,7]. In microelectronic devices, it causes steps to appear between initially level surfaces of adjoining thin film components such as metal-interconnect lines and polymer-based dielectric structures [4,9]. Indirect evidence of interfacial creep has also been obtained in dispersion-strengthened metals (e.g., [10,11]), eutectic alloys [12,13], intermetallics [14], and discontinuously reinforced composites [15–19], although the effect of interfacial creep is often difficult to recognize because of other concurrent and superposed phenomena (such as creep of one of the components adjoining the interface).

Historically, interfacial creep, which produces relative displacements between adjacent components in the absence of interfacial de-cohesion, has been thought of in a number of different ways. The various mechanisms considered include: (a) *diffusional creep* with either diffusion or interface-reaction control [10,20], as observed at phase-boundaries in eutectic alloys [13], film-substrate interfaces [5–7], and interfaces in metal-matrix composites [2,3,17]; (b) *power-law creep* within a narrow, highly dislocated interfacial region, as in fibrous metallic composites [15,16]; (c) a combination of *shear-driven viscous drag and normal stress gradient driven diffusional flow*, with both mechanisms displaying linear stress dependencies, as in whisker-reinforced metallic composites [18,19]; and (d) thermally activated *cooperative glide of intrinsic interface dislocations*, as along γ/α_2 phase boundaries in TiAl [14]. Thus, a definitive mechanistic basis for interfacial sliding has been elusive. This is perhaps not surprising, since in most studies to date, the kinetics of interfacial sliding has been inferred from the overall strain response of complex materials systems, which typically comprise several superposing effects.

In order to address this, Funn and Dutta [21] designed an experimental approach to study interfacial creep in isolation from other concurrent effects, using a fiber-pushdown approach on model single fiber composites (SFC). By loading the interface uniformly in shear, and directly measuring the relative displacement between the matrix and fiber during steady state sliding under constant push-down loads, it was determined that the interface slid by *interface-diffusion-controlled diffusional creep*. The basic mechanism is akin to that of grain boundary sliding [22], where applied far-field stresses causes normal stress gradients at the interface due to topographical variations, allowing mass transport, and hence sliding, along the interfaces. It was shown that the interfacial shear displacement rate due to sliding is given by [21]:

$$\bar{U} = \frac{4\delta_i D_i \Omega}{kTh^2}\left[\tau_i + 2\pi^3\left(\frac{h}{\lambda}\right)^3 \sigma_n\right] \quad (1)$$

where δ_i and D_i are the interfacial thickness and diffusivity, respectively, Ω is the atomic volume of the diffusing species, λ and h are the topographical periodicity and roughness of the interface respectively, and k, R, and T have the usual meanings. The resulting shear strain rate is given by $\bar{\gamma}_i = \bar{U}/h$. The interfacial shear stress τ_i is the primary driving force for this process, which is enhanced if a far-field tensile normal interfacial stress σ_n is present (i.e., positive σ_n), or reduced if there is a compressive σ_n (negative σ_n). Since $\bar{U} \propto h^{-2}$, a smooth interface would slide more readily.

Recently obtained data, based on experiments on planar Al-Si interfaces [23], were consistent with the interfacial creep model proposed in [3], although detailed parametric dependencies of the creep kinetics on material and loading variables were not reported. In this paper, we report detailed results of well-controlled interfacial creep experiments conducted on Al-Si, with the aim of verifying the validity of Eq. (1), and providing additional insight into the operative mechanism(s) of diffusionally accommodated interfacial sliding.

2. Experimental approach

Al-Si-Al sandwich structures were fabricated from 99.9% pure polycrystalline Al and undoped, single crystal <100> Si by diffusion bonding in vacuum (10^{-6} torr) at a temperature, applied pressure and time of 838 K, 1.6 MPa and 1 h, respectively. Because of the limited mutual solid solubility, the Al-Si interfaces thus produced were relatively sharp, and yet well bonded. Prior to diffusion bonding, the Al and Si surfaces to be bonded were metallographically polished and sequentially cleaned and degreased in ethanol, trichloroethylene, acetone and isopropyl alcohol, following standard microelectronic processing practice. After diffusion bonding, the sandwich structure was cooled very slowly (~ 2 K/min) in order to minimize thermally induced residual stresses at the Al-Si interfaces. In order to vary the interfacial topography (i.e., the parameters h and λ in Eq. (1)), the Si surfaces were metallographically prepared to a final nominal polish of either 1, 5, or 17 μm, producing RMS roughnesses of 15, 50 and 166 nm, respectively, as measured by atomic force microscopy (AFM) [24]. The corresponding maximum roughnesses (with 90% confidence) were computed to be 18, 54 and 174 nm, respectively. It was assumed that the final topography of the Al-Si interface is determined by the surface topography of the hard, undeformable Si. Thus, the h values for the samples with the three different surface preparation were taken to be 18, 54 and 174 nm, with associated h/λ values of 0.16, 0.21 and 0.23, respectively (Table 1). Additional details of sample fabrication and characterization are given in [24].

Table 1
Parameters describing interfacial topography for the three sample sets

Sample set	Interfacial roughness, h(nm)	Interfacial roughness/periodicity, h/λ
1	18	0.16
2	54	0.21
3	174	0.23

The sandwich structure was subsequently sectioned to produce 45 × 6 × 6 mm test samples (Fig. 1), and the sample surfaces were ground to 5 μm. The samples were then mounted on a slotted specimen platform with the 6 mm wide Si centered precisely on the 7 mm wide slot. A tungsten plate indenter, connected to a servo-hydraulic MTS frame equipped with an appropriate load cell (0.1 N resolution) was utilized to apply a constant load to the top of the Si layer. This arrangement allowed the two Al-Si interfaces to be loaded in shear, τ_i being the mean shear stress acting on each interface. For some of the samples, the interfaces were subjected to a normal compressive stress (in addition to τ_i), in order to evaluate the impact of a far-field interfacial normal stress σ_n and the topography parameter h/λ (see Eq. (1)). Fig. 2 shows a schematic of the specimen loading geometry. The resulting time-dependent interfacial deformation $\bar{U}$ (i.e., the relative displacement between Si and Al) was measured with a capacitance displacement gauge (0.01 μm resolution) located inside the slot in the specimen platform, just below the Si. The specimen thickness and the widths of the Si layer and the slot were optimized using finite element modeling, so as to enable uniform shear loading of

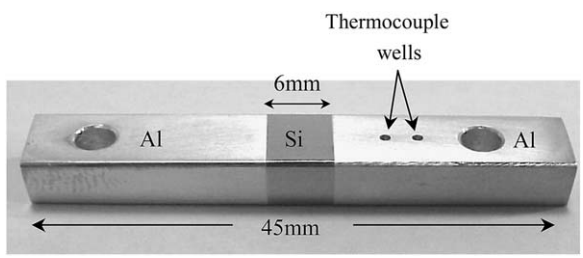

Fig. 1. Photograph of the diffusion-bonded Al-Si-Al sandwich specimen used for interfacial creep experiments.

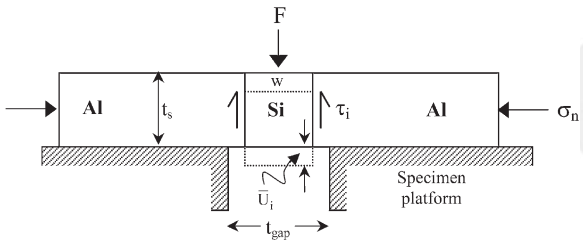

Fig. 2. Schematic of the experimental loading geometry, showing the Al-Si-Al sandwich specimen resting on a slotted platform, with the Al-Si interfaces loaded simultaneously under shear and normal stresses.

the two interfaces along the specimen thickness, while minimizing bending stresses. The sample and indenter were heated with twin-radiant heaters interfaced with a proportional controller, which allowed maintenance of the temperature with an accuracy of ±0.5 K. The entire set-up was enclosed in an environmental chamber with a slight positive pressure of forming gas (98%Argon/2%H_2) during testing. All creep experiments were conducted at loads well under those required to cause interfacial de-cohesion or fracture at the relevant temperature.

The structure and chemistry of the interface prior to, and following creep, were studied using high resolution transmission electron microscopy (HREM) on cross-sectional samples. For this, 250 μm thick slices were cut from the Al-Si-Al sandwich specimens perpendicular to the interface, and ground on both sides to a thickness of 80 μm using SiC abrasive of 5 μm grit size. These samples were then dimple-ground to 2–5 μm thickness using 1 μm diamond paste, and subsequently ion-milled in a cold-stage at 6 keV and 0.5 mA at 12° tilt for approximately 8 h. The Al-Si interface was then inspected in a TEM at an accelerating voltage of 300 keV, with the interfacial plane parallel to the electron beam.

3. Results

3.1. Observation of interfacial creep

Typical creep curves obtained from the interface creep test are shown in Fig. 3. In all cases, steady state was established within ~300–400 min. This

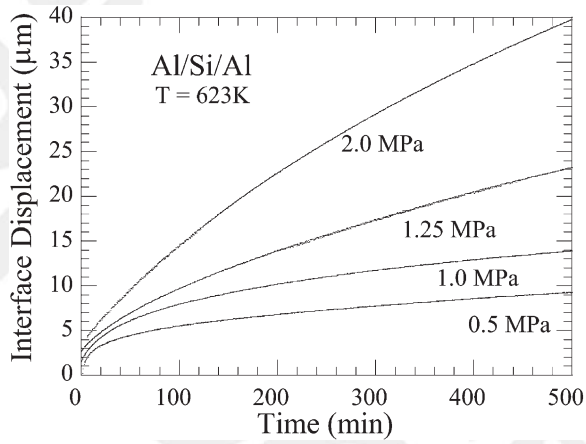

Fig. 3. Example of interfacial creep curves for various applied shear stresses τ_i at 623 K with the normal stress $\sigma_n = 0$.

steady state continued for a long time (at least 24 h at all tested temperatures and loads), until enough of the Si emerged from the bottom so that the associated reduction in interfacial area resulted in an appreciable increase in τ_i.

Fig. 4 illustrates the displacement obtained at the Al-Si interface after being subjected to a creep test for 4 h at 573 K and a mean interfacial shear stress (τ_i) of 1 MPa, as revealed by a grid pattern of nominally 5 μm diameter circles evaporated across the interface in one of the samples. Evidently, all deformation was confined to the interface only,

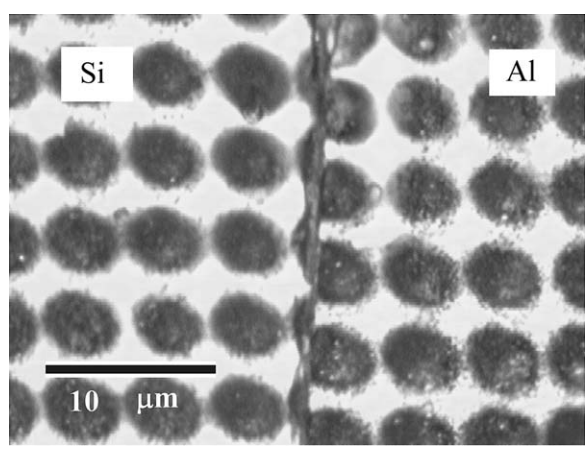

Fig. 4. Micrograph showing misalignment of rows of Al grid pattern deposited across an Al/Si interface following creep testing at 1 MPa and 573 K for 4 h.

with negligible deformation in either Si or Al. The observed displacement was uniform along the entire interface, and consistent with the measured creep displacement. No evidence of interfacial decohesion was noted. In addition, orientation imaging microscopy (OIM) within the first layer of Al grains next to the interface before and after creep tests revealed no evidence of Al lattice curvature or textural differences [24], suggesting that the displacement observed in Fig. 4 is confined to the interface. Thus, the experimental approach is clearly able to isolate and measure interfacial creep displacements.

3.2. Constitutive behavior without far-field normal stress

Fig. 5 shows a plot of the average interfacial displacement rate ($\bar{U}$) as a function of τ_i for the sample with $h = 18$ nm and $\sigma_n = 0$. Over the entire temperature range of testing ($0.45T_m$–$0.72T_m$ of Al), $\bar{U}$ displays linear stress dependence, with the creep rate vanishing at zero interfacial shear stress ($\tau_i = 0$). Fig. 6 shows a plot of $\ln\bar{U}$ vs. 1/T for τ_i levels ranging from 0.25–2 MPa, also for $h = 18$ nm and $\sigma_n = 0$. All the curves yield the same nominal slope, yielding an apparent activation energy (Q_{app}) of ~42 kJ/mole for all testing conditions.

Eq. (1) may be rewritten as:

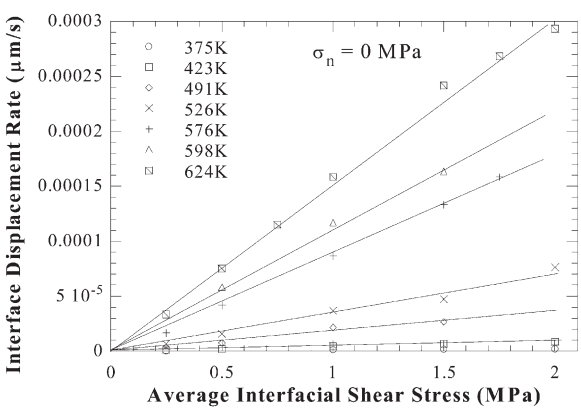

Fig. 5. Average steady state interfacial displacement rate ($\bar{U}$) as a function of applied average interfacial shear stress (τ_i) with no interfacial normal stress applied ($\sigma_n = 0$). The system exhibits linear stress dependence with no threshold stress.

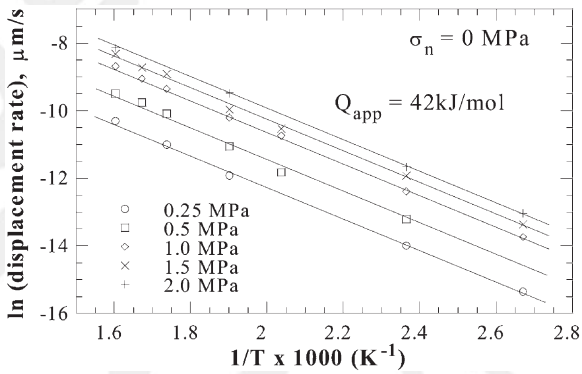

Fig. 6. Dependence of interfacial displacement rate on temperature in the absence of far-field normal stsress ($\sigma_n = 0$). An apparent activation energy of ~42 kJ/mol is computed.

$$\frac{\bar{U}kT}{\exp\left[-\frac{Q_i}{RT}\right]} = \frac{4\delta_i D_{io}\Omega}{h^2}\left[\tau_i + 2\pi^3\left(\frac{h}{\lambda}\right)^3\sigma_n\right] \quad (2a)$$

or

$$\frac{\bar{U}kT}{\left[\tau_i + 2\pi^3\left(\frac{h}{\lambda}\right)^3\sigma_n\right]} = \frac{4\delta_i D_{io}\Omega}{h^2}\exp\left[-\frac{Q_i}{RT}\right] \quad (2b)$$

where the left hand side (LHS) in Eq. (2a) represents the temperature-compensated interfacial displacement rate (TCIDR), the LHS in Eq. (2b) represents the stress-compensated interfacial displacement rate (SCIDR), and D_{io} and Q_i are the frequency factor and activation energy, respectively, for the relevant diffusion process. When the applied interfacial normal stress $\sigma_n = 0$, these reduce to:

$$\frac{\bar{U}kT}{\exp\left[-\frac{Q_i}{RT}\right]} = \frac{4\delta_i D_{io}\Omega}{h^2}\tau_i \quad (3a)$$

and

$$\frac{\bar{U}kT}{\tau_i} = \frac{4\delta_i D_{io}\Omega}{h^2}\exp\left[-\frac{Q_i}{RT}\right] \quad (3b)$$

Figs 7 and 8 show plots of TCIDR vs. τ_i and ln(SCIDR) vs. $1/T$ (Eqs (3a) and (3b)), based on the data shown in Fig. 5, and assuming $Q_i = Q_{app} = 42$ kJ/mole. All the data fall on straight

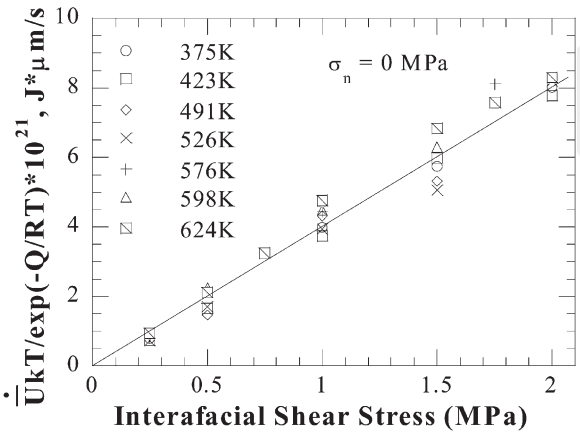

Fig. 7. Temperature-compensated interfacial displacement rate as a function of interfacial shear stress, plotted for all tests with $\sigma_n = 0$. The same creep law, with a linear stress dependence, is obeyed under all conditions.

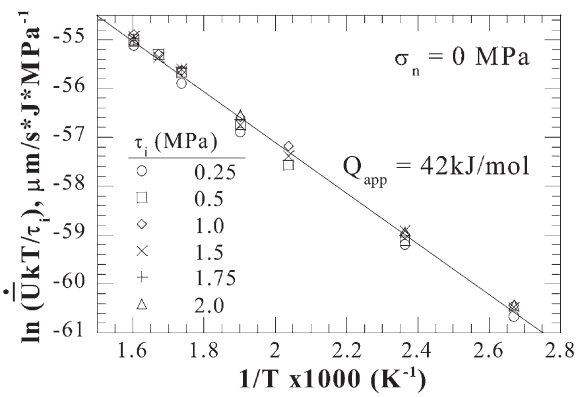

Fig. 8. Stress-compensated interfacial displacement rate as a function of temperature, plotted for all tests with $\sigma_n = 0$. The same creep law, with a an apparent activation energy Q_{app} of 42 kJ/mol, is obeyed under all conditions.

lines in both plots, displaying excellent agreement with Eq. (1). Clearly, the same mechanism of interfacial creep operates over the entire test range (T/T_m of 0.45–0.72 and τ_i/G of ~2×10^{-5}–2×10^{-4}, G being the shear modulus of Al) for $\sigma_n = 0$.

3.3. Role of far-field normal stress

Fig. 9 shows the effect of applying a normal compressive stress σ_n in conjunction with τ_i on the creep behavior of the interface. With $\sigma_n = 0$, the steady state displacement rate at $\tau_i = 1$ MPa and 623 K is ~1.5×10^{-4} μm/s. Upon superimposing a σ_n, the creep rate is appreciably smaller, but increases as σ_n is decreased, and returns to 1.5×10^{-4} μm/s when σ_n returns to zero. Figs 10(a) and (b) plot $\bar{U}$ against τ_i at 623 and 523 K, and 523 and 423K, respectively, for various applied normal compressive stresses ($\sigma_n = 0$, −0.6, −1.5, and −3.0 MPa). When a compressive σ_n is imposed, the interfacial displacement rate ($\bar{U}$) at a given τ_i decreases. Readily apparent is the emergence of a clear threshold behavior (i.e., a shear stress value τ_o below which the interface does not creep) when $\sigma_n \neq 0$. A σ_n of greater magnitude results in a larger threshold stress τ_o, which is identical at all temperatures for a given σ_n value. Thus, the threshold stress τ_o appears to be temperature-independent.

Fig. 11 shows a plot of the temperature-compensated interfacial displacement rate, TCIDR, vs. τ_i, for all test conditions, including both $\sigma_n = 0$ and $\sigma_n \neq 0$. The computation of TCIDR assumed an activation energy of 42 kJ/mole. It is readily apparent that the data for all test temperatures at each value of σ_n are co-linear. Increasing the magnitude of σ_n increases the threshold stress τ_o below which interfacial creep does not occur, but does not change the slope of the straight-line plot, which represents the creep coefficient $A_i = \left(\frac{4\delta_i D_{io}\Omega}{h^2}\right)$ in Eq. (2a). The parallelism of the plots, coupled with the co-linearity of the data for all temperatures at each σ_n value, clearly indicate that the creep mechanism is independent of temperature and σ_n, the only effect of σ_n being to increase the observed threshold stress. Based on Eq. (2a), it is apparent that for a compressive (i.e., negative) σ_n, the threshold stress is given by:

$$\tau_o = 2\pi^3\left(\frac{h}{\lambda}\right)^3 |\sigma_n| \qquad (4)$$

and is thus independent of temperature, as noted experimentally. Thus, the applied normal compressive stress simply serves to reduce the effective shear stress, which drives interfacial creep, from $\tau_i - \tau_{eff} = (\tau_i - \tau_o)$, thereby reducing the creep rate.

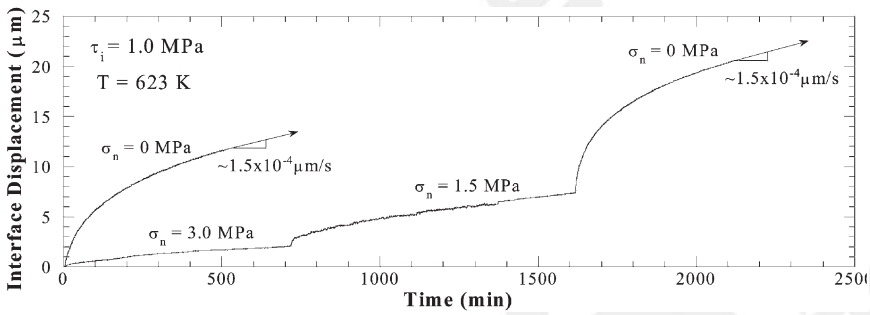

Fig. 9. Creep curves showing the effect of applied normal compressive stress σ_n on interfacial displacement at a constant applied shear stress (τ_i =1.0 MPa) and temperature (623 K). The application of $\sigma_n = -3$ MPa decreases the steady state creep rate, which increases as the magnitude of σ_n is reduced.

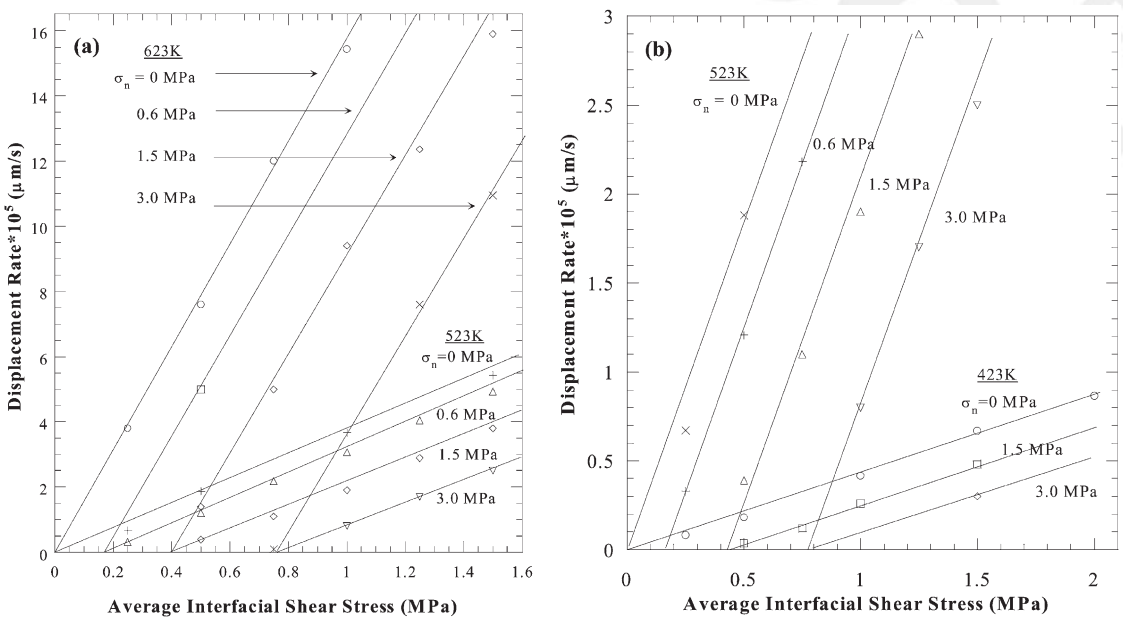

Fig. 10. Interfacial displacement rate as a function of τ_i at various levels of applied interfacial normal stresses σ_n at (a) 623 and 523 K, and (b) 523 and 423 K. Two separate figures (a) and (b) have been used because of the wide range of interfacial displacement rates represented. A threshold stress τ_o, which depends on σ_n, is clearly noted in both figures.

Fig. 12 plots the interfacial displacement rate, compensated by the appropriate τ_{eff} values (computed using the experimentally obtained τ_o values from Fig. 11), against reciprocal temperature ($1/T$). Upon compensating for the differing threshold stress, all data points become co-linear. Clearly, independent of the applied normal stress, the interface creeps via the same mechanism under all conditions, with Q = 42 kJ/mole.

From Fig. 11, the threshold stress τ_o for σ_n values of 0.6, 1.5 and 3 MPa are determined to be 0.16, 0.39, and 0.77 MPa, respectively. Using these values in conjunction with Eq. (4), the ratio h/λ is computed to be ~0.16 in all cases. This is almost identical to the h/λ value of 0.16 estimated based on AFM measurements on the Si-surface prior to diffusion-bonding (Table 1). The consistent value of h/λ obtained from the experiments with different applied σ_n values suggests that the functional relationship between τ_o, σ_n and h/λ, as given by Eq. (4), i.e., $\tau_o \propto \sigma_n (h/\lambda)^3$, is correct.

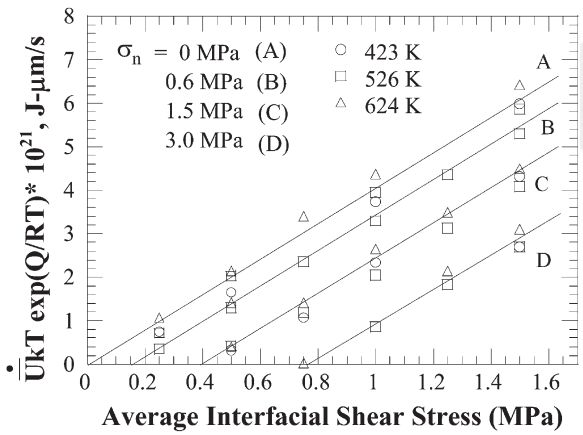

Fig. 11. Temperature-compensated interfacial displacement rate vs. τ_i for various σ_n values, showing mechanistically identical creep behavior under all conditions, but with a threshold stress τ_o which clearly depends on σ_n. It is clear that τ_o is temperature-independent.

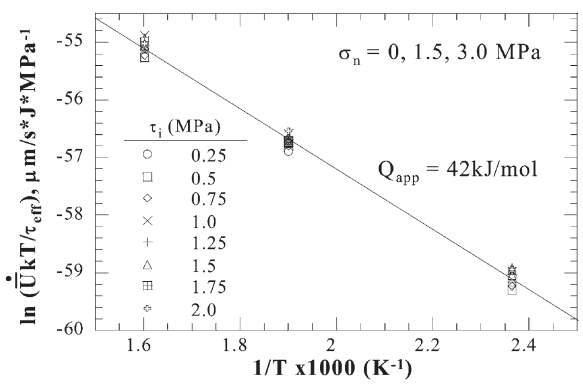

Fig. 12. Plot of interfacial displacement rate, compensated by the effective stress τ_{eff}($= \tau_i - \tau_o$), against temperature for all experimental conditions (including both $\sigma_n = 0$ and $\sigma_n \neq 0$). The same mechanism operates under all conditions, with Q_{app} = 42 kJ/mole .

3.4. Role of interfacial roughness

In order to clearly establish the effect of interfacial topography on the creep coefficient A_i and the threshold stress τ_o, experiments were conducted at different h and h/λ values. Fig. 13 shows plots of the steady state displacement rate vs. τ_i for three different interfacial topographies (h = 18, 54 and 174 nm) at 624 K and $\sigma_n = 0$. As expected, the creep rate decreases sharply with increase in

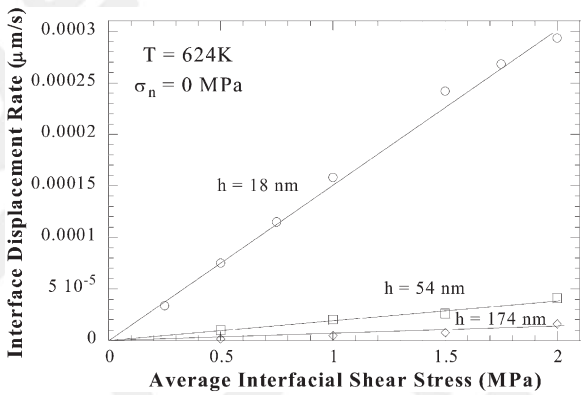

Fig. 13. Interfacial displacement rate $\bar{U}$ as a function of τ_i, with $\sigma_n = 0$ for three interfacial roughnesses (h = 18, 54 and 174 nm). A linear stress dependence is observed, with no threshold stress. $\bar{U}$ decreases sharply with increase in h.

interfacial roughness h, but the same linear stress dependence prevails for all topographies. In Fig. 14, the interfacial displacement rate is plotted against $1/h^2$ and λ/h^2 for various τ_i. It is observed that $\bar{U}$, and hence the creep constant A_i, is proportional to $1/h^2$, as suggested by Eq. (1) (i.e., $A_i = \left(\frac{4\delta_i D_{io}\Omega}{h^2}\right)$). Contrarily, $\bar{U}$ is clearly non-linear with respect to λ/h^2. The significance of this will be discussed in section 4.

Fig. 15 shows a plot of $\bar{U}$ vs. τ_i at 624 K for varying interfacial topographies and σ_n. Several points emerge from this plot. First, as noted in Fig. 13, when $\sigma_n = 0$, increasing h reduces $\bar{U}$, lowering the slope of the plot, although the lines converge at $\tau_i = 0$. Secondly, at a given h (e.g., 18 nm), increasing the magnitude of σ_n results in an increasing threshold stress τ_o, but the $\bar{U}$ vs. τ_i plots remain parallel. The same is true for other values of h. Thirdly, it is noted that at a given value of σ_n (e.g., −1.5 MPa), the slope of the $\bar{U}$ vs. τ_i plot decreases as h is increased. Importantly, it is noted that the threshold stress τ_o increases as h increases. No meaningful data could be obtained for h = 174 nm with $\sigma_n = -3$ MPa, since the creep rates were too low to be measurable in a reasonable time (~72 h). This is most likely because τ_o was close to 2 MPa (or greater) for $\sigma_n = -1.5$ MPa, and increasing τ_i to much more than 2 MPa induced deformation of the Al immediately next to the interface,

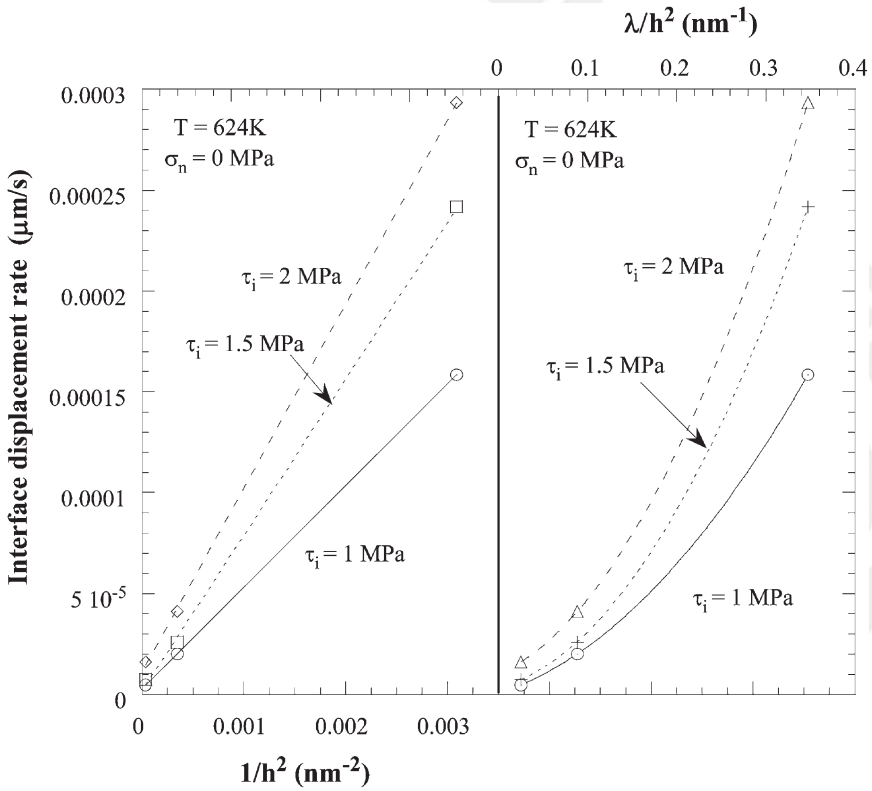

Fig. 14. Plots of $\bar{U}$ vs. $1/h^2$ and λ/h^2. The interfacial displacement rate is inversely proportional to h^2 at all levels of τ_i, but has a non-linear dependence on λ/h^2.

with much greater creep kinetics. This was evidenced by the observation that at applied stresses of 2.5 MPa and beyond, $\bar{U}$ increased rapidly, with the $\bar{U}$ vs. τ_i plot becoming non-linear, and nominally independent of h and σ_n. Thus the current experimental conditions allowed isolation of interfacial creep from creep of Al only below ~2 MPa. Because of this, the reported data are limited to $\tau_i \leq 2$ MPa.

Using Eq. (4), the values for τ_o may be calculated for the samples with h = 54 nm, assuming that h/λ = 0.21, as per Table 1. For $\sigma_n = -1.5$ MPa, this yields τ_o = 0.86 MPa, and for $\sigma_n = -3$ MPa, τ_o = 1.72 MPa. These values are different from, but close to the experimental values of 0.9 and 1.5 MPa, respectively, as determined from Fig. 15. Likewise, the computed τ_o value for the sample with h = 174 nm (h/λ = 0.23) is computed to be 1.1 MPa, which is slightly different from the experimentally obtained value of 1 MPa. It should be realized that there is some uncertainty in the experimentally determined τ_o values because of the limited number of data points available. Furthermore, although the experimental h value can be determined with fair accuracy from the roughness distributions measured via AFM, the corresponding values of h/λ are difficult to measure accurately because of the inherent uncertainty in measuring λ, this difficulty increasing with higher roughness values. In light of these uncertainties, the closeness of the measured and predicted τ_o values are deemed to provide reasonable validation of the functional dependency of τ_o on σ_n and h/λ, as predicted by the model.

3.5. Interfacial structure

Figs 16 and 17 show HREM images of the interface in the as-fabricated condition, and after pro-

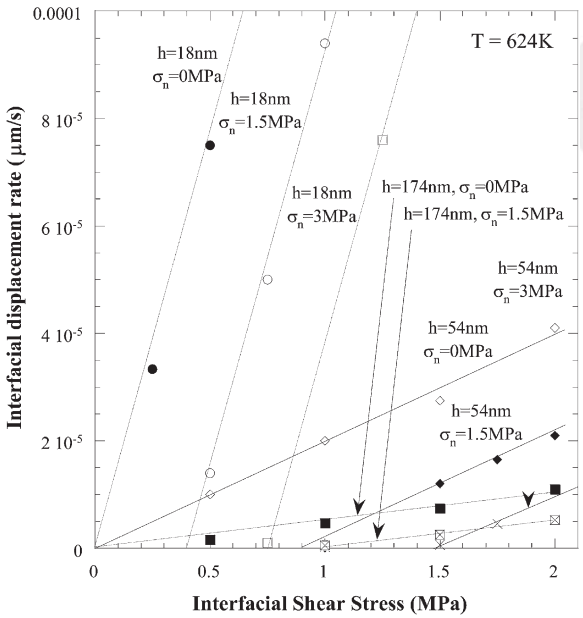

Fig. 15. Interfacial displacement rate as a function of applied interfacial shear stress when an interfacial normal stress is applied showing a linear shear stress dependence with an observed threshold stress. Observed threshold stress increases with increasing applied interfacial normal stress and interfacial roughness.

longed creep at 624 K. An amorphous layer, nominally ~20 nm wide, was present at the Al-Si interface prior to testing. The actual thickness of this layer varied considerably along the interface, being only a few nanometers in certain regions, and as thick as 60 nm in others. Fig. 16 shows HREM images of the Si and Al sides of the interface, along with the computed fast Fourier transforms (FFT) of the lattice images. The Si side of the interface displays a relatively sharp transition to the amorphous region, which is situated almost entirely on the Al side, showing a gradual transition to crystalline Al. This is clear from the FFT pattern from the apparently crystalline part of Al, which shows that the spots due to the lattice planes are superimposed by a diffuse intensity due to the amorphous character. Energy dispersive X-ray spectroscopy (EDXS) confirmed that the amorphous layer is Al with a high (non-equilibrium) amount of dissolved solutes. Of these, oxygen was the predominant component, although the amount of dissolved Si was also high. Trace amounts of S, possibly due to dissociation of the MoS_2 die-lubricant used during diffusion-bonding, was also found in this region. Amorphous layers on the order of a few to several tens of nanometers thick are frequently observed at interfaces in both bulk and thin film systems with either Al/Al_2O_3 or Si/SiC on one side [24–28]. This is typically associated with adsorbed oxygen and/or nascent oxide layers on the surfaces of Si and Al [27], consistent with the high oxygen concentration observed in the present work.

After thermo-mechanical exposure, numerous nano-crystallites, ~6–10 nm in size, emerged within the amorphous layer on both the Al and Si sides. This is shown in Fig. 17, which represents the structure of the interface after prolonged creep testing (~24 h) at 624 K and τ_i = 1.5 MPa. The amorphous region is noted to have shrunk considerably (to a thickness on the order of 10 nm), having been consumed from both the Al and Si sides by the formation of contiguous nano-scale crystallites. Compositional analysis by EDXS revealed that the crystallites formed on the Al side of the amorphous zone were predominantly Al region 1 in Fig. 17), whereas those formed on the Si side were predominantly Si (region 2). Clearly, thermo-mechanical loading allowed these Al and Si rich nano-crystallites to nucleate within the amorphous region, next to the crystalline Al and Si, respectively. Commensurate with the formation of nearly pure Al and Si crystallites from the two sides, the residual amorphous zone became increasingly enriched in solute (mainly oxygen, region 3). Thus, the structure and composition of the amorphous region evolved during creep testing.

Although the creep testing temperatures (maximum of 624 K) are significantly below the diffusion bonding temperature for the present samples (838 K), it is only during testing that the observed crystallization occurred, highlighting the combined roles of interfacial shear stress and temperature. Indeed, deformation-induced crystallization of amorphous metallic alloys below the glass transition temperature (T_g) has been noted earlier [29–31], and has been variously attributed to adiabatic heating induced short-range atomic rearrangement [29], locally enhanced atomic diffusion due to flow dilatation [30], or local hydro-

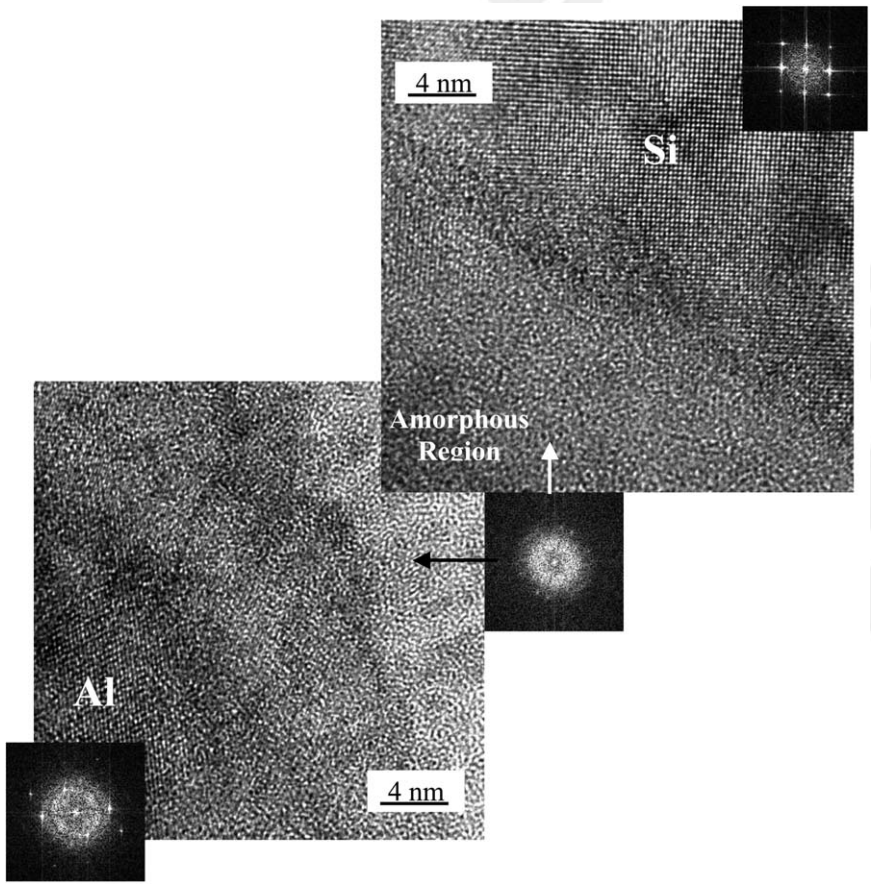

Fig. 16. HREM image and corresponding fast Fourier transforms of the Al-Si interfacial region. The interface comprises a 20–40 nm wide amorphous Al region, high in solute concentration, between crystalline Al and Si.

static pressure induced alteration of crystallization temperature [31]. The precise reason for the crystallization observed in the present work is unclear, but it is readily apparent that it results in compositional changes within the amorphous interfacial zone as testing progresses.

4. Discussion

In the present experiments, Si is not expected to display creep at the relevant temperatures. Therefore, the experimentally measured deformation occurs either at the interface or in a narrow band of Al immediately adjacent to the interface. However, under the stress/temperature conditions of interest, grain boundary diffusion controlled Coble creep would be the only mechanism yielding measurable strain rates in Al [32]. While this would explain the observed linear stress dependence, it would yield an activation energy value commensurate with that of grain boundary diffusion in Al, i.e., Q_{gb} = 84 kJ/mole, which is about twice the value of the measured Q_{app}. Furthermore, given that the grain sizes in Al immediately adjacent to the interface were ~40–60 μm [24], Coble creep would not result in the very narrow deformation band indicated by Fig. 3. Besides, the Coble creep rate of Al over most of the test conditions would be ~10^{-10}–10^{-8}/s, far below the equivalent strain rates of ~10^{-3}/s, which may be estimated assuming that Al deforms within a ~0.1 μm thick band next to the

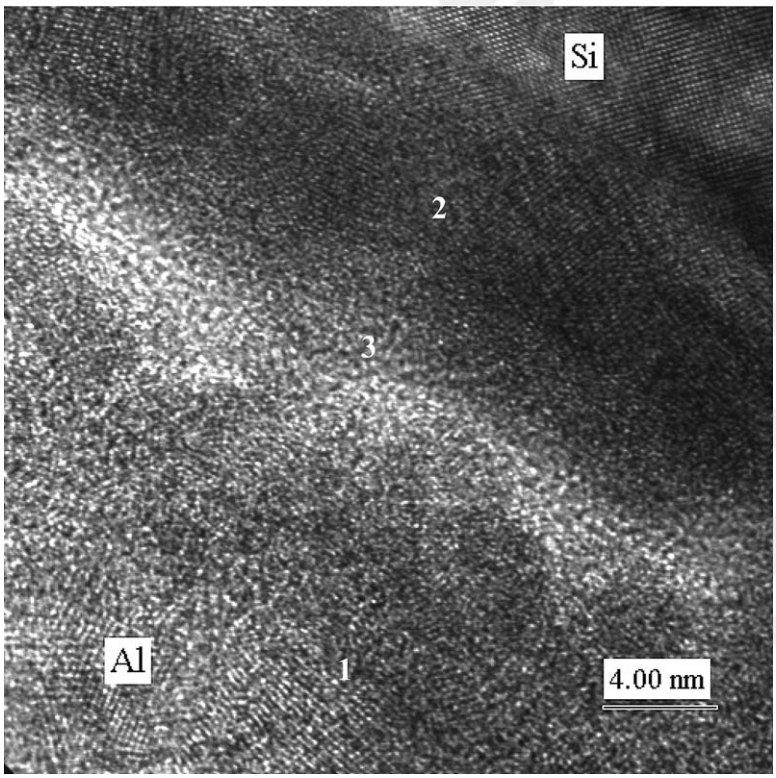

Fig. 17. HREM image of the interface after creep testing for 24 h at 624 K and τ_i =1.5 MPa. Crystallization has occurred from both Al and Si sides (regions 1 and 2) of the amorphous Al region. This results in shrinkage of the amorphous region, which becomes more highly concentrated with solute (region 3).

interface. Therefore it can be inferred that the observed creep deformation is not due to Al at all, but rather, must be occurring at the interface, thereby establishing the efficacy of the present approach in isolating the intrinsic interfacial behavior.

By examining the literature, one can conclude that there are two situations where interfacial creep may occur with little or no matrix deformation, as in this study. First, interfacial sliding may occur by diffusional creep [21,22]. When the interface acts as a perfect source and sink of vacancies, e.g., due to an abundance of mobile boundary dislocations (BDs), the stress exponent $n = 1$, and Q equals that for either boundary or lattice diffusion, and the process is "diffusion controlled" [10,22]. When the density or mobility or dislocations in the boundary is limited, on the other hand, the kinetics of sliding are believed to become "interface reaction controlled", resulting in n~2, a threshold stress corresponding to the minimum stress required to move BDs, and a high activation energy associated with rearranging atoms on the more refractory/stiffer side of the interface [10,20]. However, in the present study, $n = 1$, Q is low, and a threshold stress is not observed, suggesting that the observed sliding is not interface-reaction controlled.

Another mechanism which would lead to $n \approx 1$ is cooperative glide of intrinsic interface dislocations (ID), which has been thought to cause sliding at γ/α_2 phase boundaries in TiAl in the low stress/intermediate temperature regime [14]. Here, the glide rate is thought to be limited by climb of sessile jogs and/or solute drag from interstitial impurities on the interface plane, giving rise to a thermally activated process.

Based on the above, the data obtained here could

be rationalized by either diffusion-controlled diffusional creep or viscous glide of interface dislocations. However, the presence of the amorphous interfacial layer, as observed via HREM, suggests that the dislocation-based viscous glide model suggested in [14] is not applicable here. Further, the Q values obtained in the present experiments are not consistent with either climb of jogs (which would produce $Q \approx Q_{vol}$ for Al = 142 kJ/mol), or solute diffusion ($Q \approx Q_{Si}$ in Al ~ 123–136 kJ/mol) [33], which would be needed for glide of interfacial dislocations. It is therefore proposed that the mechanism of interfacial sliding in the present studies is 'interface diffusion-controlled' diffusional creep, identical to that observed in [8], and described by Eq. (1).

When a far-field shear stress is applied to the interface, the interfacial roughness results in a periodically varying normal stress at the interface, which drives diffusive flux of Al through the interface, producing a relative displacement of Si and Al [21]. The simultaneous application of far-field shear and normal stresses results in local normal stresses at the interface with different periodicities [21], resulting in a threshold behavior when the normal stress is compressive, or an enhancement of the creep rate if the normal stress is tensile.

The specific path of "interfacial diffusion" is not clear, but may be surmised from the observed Q value of 42 kJ/mole. Creep studies conducted on several amorphous Al alloys [34] have shown that below the glass transition temperature T_g, creep occurs by diffusional flow of Al in the glass with Q ~ 24–45 kJ/mol, whereas above T_g, deformation occurs by viscous flow of the supercooled liquid with Q ~ 188–328 kJ/mol. This is consistent with the hypotheses that diffusional flow below T_g occurs by fast atomic diffusion through a relatively open amorphous structure leading to a low Q, whereas viscous flow above T_g requires movement of volumes of short-range ordered atoms in the supercooled liquid past other such volumes, producing a higher Q [35,36]. The Q value of 42 kJ/mol obtained in the present study is consistent with solid-state diffusion of Al in amorphous Al below T_g, and therefore it is inferred that even at the highest testing temperature, T_g of the interfacial layer is not exceeded. An interfacial sliding mechanism based on viscous flow of the amorphous phase above T_g may be further discounted, realizing that this can only occur when the interfacial roughness is significantly smaller than the amorphous layer thickness—a condition which is not valid for at least some of the samples used here (i.e., h = 54 and 174 nm).

The experiments suggest that the interfacial roughness h is adequately described by surface roughness measurements on Si prior to bonding. The results clearly demonstrate that the kinetics of sliding varies as $1/h^2$, which is associated with "interfacial diffusion". This is clear from Fig. 14, which also shows that the $\bar{U}$ vs. λ/h^2 plot is distinctly non-linear. Previous analytical modeling of interfacial creep [21] has shown that when only one side of the interface is at a high homologous temperature (as in the present case of Al/Si), the total sliding rate is given by the sum of the contributions due to (a) interfacial diffusion and (b) diffusion through the less refractory side. The total rate may therefore be written as [21]:

$$\bar{U} = \frac{4\delta_i D_i \Omega}{kT}\left(\frac{1}{h^2}\right)\left[\tau_i + 2\pi^3\left(\frac{h}{\lambda}\right)^3\sigma_n\right] + \frac{2D_m^{eff}\,\Omega}{kT\,\pi}\left(\frac{\lambda}{h^2}\right)\left[\tau_i + \pi^3\left(\frac{h}{\lambda}\right)^3\sigma_n\right] \quad (5)$$

where the second term represents the contribution of bulk and/or grain boundary diffusion through the less refractory side of the interface (in this case, Al), D_m^{eff} being the associated effective diffusivity. When interfacial diffusion dominates, the first term is predominant, and Eq. (5) devolves to Eq. (1), making $\bar{U} \propto 1/h^2$. If, on the other hand, sliding is dominated by bulk diffusion through one side of the interface, $\bar{U} \propto \lambda/h^2$. The linearity of the $\bar{U}$ vs. $1/h^2$ plot, and the non-linearity of the $\bar{U}$ vs. λ/h^2 plot in Fig. 14 clearly establishes that in the present experiments, sliding is dominated by interfacial diffusion, as opposed to bulk diffusion through one side of the interface. This is despite the fact that the diffusion path seems to be through the amorphous interfacial layer, as noted above. This suggests that the effective thickness of the amorphous layer through which "interfacial diffusion" occurs (i.e., the "interfacial thickness" δ_i) is much smaller than the h value for the associated interface, thereby

allowing the amorphous layer to act as an integral part of the interface instead of behaving like a separate phase. It appears, therefore, that the effective thickness of the interface is determined by the thinnest region of the amorphous layer, which, as indicated by HREM, varied considerably in thickness along the interface, from only a few nanometers in some regions, to a few tens of nanometers in others.

It is noted that Eq. (1) represents a steady-state mechanism, whereas the experimental results (e.g., Figs 3 and 5) show distinct primary stages in the creep curves. A primary stage is typically associated with dislocation sub-structure evolution, which is precluded in the present case since there is no evidence of dislocation activity at the interface, and the Al adjacent to the interface undergoes negligible deformation. However, as noted above, the composition of the amorphous interfacial zone evolves upon being thermo-mechanically loaded, as crystallization progresses. It is possible that this evolution of the interfacial composition is associated with evolution of the activation energy for Al diffusion through this layer, resulting in the appearance of the apparent primary stage. Indeed, creep experiments on amorphous Al alloys below T_g show substantial differences in the measured Q with alloy composition, even when the creep mechanism is the same [33]. Thus the appearance of the primary stage in the present experiments is consistent with an increasing activation energy associated with an increasing solute concentration in the amorphous region. Once the solute concentration becomes too high for crystallization to continue, the amorphous interfacial zone reaches a stable composition, and the creep curve displays a steady state as predicted in Eq. (1).

In the present mechanism, topographical variations of the interface, by giving rise to local normal stress gradients along the interface, forces Al atoms at the Si/amorphous-Al interface to diffuse through the amorphous layer in the direction of shear. The magnitude of the effective shear stress depends on both the applied shear and normal stresses, and is given by:

$$\tau_{\text{eff}} = \tau_{\text{i}} + 2\pi^3\left(\frac{h}{\bar{\lambda}}\right)^3\sigma_{\text{n}} \qquad (6)$$

where a tensile σ_n augments τ_{eff}, and a compressive σ_n reduces it by introducing a threshold behavior. Consistent with Eq. (6), the threshold stress τ_o measured in the present experiments is clearly independent of temperature, as observed in Figs 10 and 11. This is significant, since it provides an alternative rationalization for threshold behavior in diffusional creep, validating the continuum model represented by Eq. (1) [21]. Indeed, the low activation energy for creep, and the temperature independent, but normal stress dependent threshold stress observed here, clearly validate the hypothesis that a threshold behavior may be induced by a far-field normal interfacial stress, even when creep is diffusion-controlled. This is in contrast to the usual assumption of interface-reaction control, which invokes interfacial dislocation activity to rationalize the appearance of threshold behavior in diffusional creep [10]. It is worth noting that according to the present continuum model, if the interfacial normal stress becomes temperature-dependent, as in metal-matrix composites or dispersion-containing alloys, the threshold stress would also display a temperature-dependence, as observed in many systems [10,11,21].

The discussion presented earlier suggests that the presence of the amorphous layer enhances the creep rate because of the low activation energy for self-diffusion in amorphous Al. A thin amorphous layer, typically on the order of 1–5 nm, is frequently present at interfaces between dissimilar materials in both bulk and thin film systems [e.g., 25–28]. In such systems, interfacial sliding kinetics are expected to be rapid, as observed here. In thin film systems in particular, large tensile stresses (peeling stresses) are also often present near the edges, in addition to shear stresses. Therefore, in these systems, the driving force for sliding, τ_{eff}, is high, making them particularly susceptible to interfacial sliding, the effect of which would become increasingly prominent as the in-plane dimension of the film shrinks (i.e., as edge-effects become more prominent).

However, many thin film interfaces have no amorphous layer, and indeed, many are epitaxial. In these systems, the kinetics of interfacial sliding could be limited if the interfacial diffusive flux is limited by interface-reaction control [10], resulting

in a high Q_i. It is unclear whether interfacial sliding would occur to any appreciable degree in such systems.

Since the interfacial creep rate varies as $1/h^2$, very smooth interfaces like those found in microelectronic devices, where interfacial roughness h is typically <1 nm, are expected to slide quite readily, as observed in both standalone and embedded thin-film Cu interconnect lines on Si [4,6,7,9]. In these systems, the Cu lines are deposited on a 35 nm thick Ta or TaN barrier layer, and although both the Cu and the Ta/TaN are nominally crystalline, substantial sliding at the Cu/Ta interface is noted following thermal cycling, indicating that the possibly higher Q_i value for the crystalline interface is counteracted by the very small h. Experiments are currently being conducted on Al thin film/Si interfaces to understand the mechanism and impact of interfacial creep in thin film systems with crystalline interfaces.

Finally, it was noted in section 3.4. (in conjunction with the discussion of Fig. 15) that at τ_i values larger than 2 MPa, the $\bar{U}$ vs. τ_i plot became nonlinear, and apparently independent of the interfacial topography and the far-field normal stress. From this it was inferred that at high τ_i levels, interfacial creep became masked by the more rapid creep of Al immediately adjacent to the interface. As evident from Fig. 2, an approximately 0.4 mm ($\approx \frac{t_{gap} - w}{2}$) wide Al region on each side of the Si was loaded in shear in the present experimental set-up. Although at low stresses, the shear deformation of Al was negligible compared with the interfacial displacement (as evident from Fig. 4), at high τ_i values, the measured $\bar{U}$ included superposition of Al creep (power-law) on interfacial creep, resulting in anomalously high $\bar{U}$ values. This is a limitation of the experimental arrangement, and does not reflect a change in the interfacial creep mechanism at high stresses. It is therefore thought that the proposed mechanism is applicable at all levels of interfacial stress prior to fracture.

5. Conclusions

An experimental approach to isolate and measure the creep behavior of interfaces in multi-component systems was refined, and used to study model diffusion-bonded Al-Si interfaces. Experiments showed that metal-Si interfaces may undergo diffusionally accommodated sliding under shear stresses at high temperatures. The measured kinetics showed that the mechanism of sliding is interfacial diffusion-controlled diffusional flow. Like the classical grain boundary sliding mechanism [22], interfacial sliding occurs due to mass-transport under periodically varying normal stresses acting on the interface due to an applied far-field shear stress, with the mass transport path being associated with the interface. In the present experiments, Al atoms diffuse rapidly along an amorphous interfacial layer under the applied stress, leading to the observed sliding. This is consistent with a mechanism proposed earlier [21]. The kinetics of sliding varies inversely as the square of the interfacial roughness, allowing smooth interfaces (e.g., those in microelectronics) to be highly susceptible to sliding. The application of a far-field normal compressive stress influences the kinetics of sliding by introducing a temperature-independent threshold stress, the magnitude of which is dependent on the interfacial topography. A systematic parametric approach was used to validate the key components of the previously proposed model [21], which provides a continuum basis to rationalize interfacial sliding, which is observed in many multi-component systems in the absence of interfacial de-cohesion.

Acknowledgements

This work was supported by the National Science Foundation, Division of Materials Research, under Grant # DMR-0075281.

References

[1] Yoda S, Kurihara N, Wakashima K, Umekawa S. Metall Trans 1978;9A:1229.
[2] Nagarajan R, Dutta I, Funn JV, Esmele M. Mater Sci Eng 1999;A259:237.
[3] Dutta I. Acta Mater 2000;48:1055.
[4] Zhmurkin DV, Gross TS, Buchwalter LP. J Electronic Mater 1997;26:791.

[5] Jobin VC, Raj R, Phoenix SL. Acta Metall Mater 1992;40:2269–80.
[6] Chen MW, Dutta I. Appl Phys Lett 2000;77:4298.
[7] Dutta I, Chen MW, Peterson K, Shultz T. J Electronic Mater 2001;30:1537.
[8] Nix WD. Metall Trans 1989;20A:2217.
[9] Peterson KA, Park C, Dutta I. MRS Symp Proc 2002;716.
[10] Arzt E, Ashby MF, Verall RA. Acta Metall 1983;31:1977.
[11] Stang RG, Barrrett CR. Scripta Metall 1973;7:233.
[12] Ignat M, Bonnet R. Acta Metall 1983;31:1991.
[13] Gupta D, Vieregge K, Gust W. Acta Mater 1999;47:5.
[14] Hsiung LM, Nieh TG. Title. In: Baker I, Noebe RD, George EP, editors. Interstitital and substitutional solute effects in intermetallics. TMS; 1998. p. 201.
[15] Goto S, Mclean M. Acta Metall Mater 1991;39:165.
[16] Dlouhy A, Merk N, Eggeler G. Acta Metall Mater 1993;41:3245.
[17] Rosler J, Bao G, Evans AG. Acta Metall Mater 1991;39:2733.
[18] Kim KT, McMeeking RM. Mech Mater 1995;20:153.
[19] Nimmagadda PBR, Sofronis P. Mech Mater 1996;23:1.
[20] Ashby MF. Scripta Metall 1969;3:837.
[21] Funn JV, Dutta I. Acta Mater 1999;47:149.
[22] Raj R, Ashby MF. Metall Trans 1971;2:1113.
[23] Peterson KA, Dutta I, Chen MW. Scripta Mater 2002;47:649.
[24] Peterson KA, Dutta I, Chen MW. J Mater Proc Tech 2002 (in press).
[25] He X, Yang SZ, Tao K, Fan Y. Mater Lett 1997;33:175.
[26] Ye F, Lei TC, Zhou Y. Mater Sci Eng 2000;A281:305.
[27] Ratnaparkhi PL, Howe JM. Acta Metall Mater 1994;42:811.
[28] Koumninou P, Stoemenos J, Nouet G, Karakostas T. J Crystal Growth 1999;203:103.
[29] Chen H, He Y, Shiflet GJ, Poon SJ. Nature 1994;367:541.
[30] Kim JJ, Choi Y, Suresh S, Argon AS. Science 2002;295:654.
[31] Iwasaki H, Masumoto TJ. J Mater Sci 1978;13:2171.
[32] Frost HJ, Ashby MF. Deformation mechanism maps. Oxford: Pergamon Press, 1982.
[33] Brandes EA, Brook GB. Smithell's metals reference book. Oxford: Butterworth-Heinemann, 1992.
[34] Strombom J, Henderson PJ, Savage SJ. Scripta Metall Mater 1992;27:1179.
[35] Kingery WD, Bowen HK, Uhlmann DR. Introduction ceramics. John Wiley, 1976.
[36] Geiger GH, Poirier DH. Transport phenomena in metallurgy. Reading, MA: Addison-Wesley, 1980.